

## AUTHOR QUERY FORM

	<p>Journal: J. Appl. Phys. Article Number: JAP21-AR-00469</p>	<p>Please provide your responses and any corrections by annotating this PDF and uploading it to AIP's eProof website as detailed in the Welcome email.</p>
---	---	--

Dear Author,

Below are the queries associated with your article; please answer all of these queries before sending the proof back to AIP.

**Article checklist:** In order to ensure greater accuracy, please check the following and make all necessary corrections before returning your proof.

1. Is the title of your article accurate and spelled correctly?
2. Please check affiliations including spelling, completeness, and correct linking to authors. 
3. Did you remember to include acknowledgment of funding, if required, and is it accurate?

Location in article	Query / Remark: click on the Q link to navigate to the appropriate spot in the proof. There, insert your comments as a PDF annotation.
Q1	Please check that the author names are in the proper order and spelled correctly. Also, please ensure that each author's given and surnames have been correctly identified (given names are highlighted in red and surnames appear in blue). 
Q2	We were unable to locate a digital object identifier (doi) for Refs. 10 and 35.  Please verify and correct author names and journal details (journal title, volume number, page number, and year) as needed and provide the doi. If a doi is not available, no other information is needed from you. For additional information on doi's, please select this link: <a href="http://www.doi.org/">http://www.doi.org/</a> .
	<p>Please confirm ORCIDs are accurate. If you wish to add an ORCID for any author that does not have one, you may do so now. For more information on ORCID, see <a href="https://orcid.org/">https://orcid.org/</a>.</p> <p>Z. Wang M. L. Bao X. J. Wang P. K. Liaw R. P. Guo <b>J Qiao</b>—0000-0001-9119-870X</p> <p>Please check and confirm the Funder(s) and Grant Reference Number(s) provided with your submission:</p> <p>Natural Science Foundation of Shanxi Province, 201901D111105 Natural Science Foundation of Shanxi Province, 201901D111114 Transformation of Scientific and Technological Achievements Programs of Higher Education Institutions in Shanxi, 2019 State Key Laboratory of Explosion Science and Technology, KFJJ20-13M China Postdoctoral Science Foundation, 2020M670708 US Army Research Office, W911NF-13-1-0438 US Army Research Office, W911NF-19-2-0049 National Science Foundation, DMR-1611180 National Science Foundation, DMR-1809640</p> <p>Please add any additional funding sources not stated above:</p>

Thank you for your assistance.

# 1 Deformation mechanisms in hexagonal close-packed high-entropy alloys

2  
 3 Cite as: J. Appl. Phys. **129**, 000000 (2021); doi: [10.1063/5.0045414](https://doi.org/10.1063/5.0045414)

4 Submitted: 26 January 2021 · Accepted: 19 April 2021 ·

5 Published Online: ■■■ 2021



Q1

6 Z. Wang,<sup>1,2</sup> M. L. Bao,<sup>1</sup> X. J. Wang,<sup>1</sup> P. K. Liaw,<sup>3</sup> R. P. Guo,<sup>1</sup> and J. W. Qiao<sup>1,a)</sup>

## 7 AFFILIATIONS

8 <sup>1</sup>College of Materials Science and Engineering, Taiyuan University of Technology, Taiyuan 030024, China

9 <sup>2</sup>Department of Engineering, Lancaster University, Lancaster, LA1 4YW, United Kingdom

10 <sup>3</sup>Department of Materials Science and Engineering, The University of Tennessee, Knoxville, Tennessee 37996-2200, USA

11

12 a)<sup>a</sup>Author to whom correspondence should be addressed: [qiaojunwei@gmail.com](mailto:qiaojunwei@gmail.com)

13

## 14 ABSTRACT

15 Single-phase hexagonal close-packed structure of the ScYLaGdTbDyHoErLu high-entropy alloy was studied in detail. The applicability of the  
 16 rule of mixture was analyzed with respect to the lattice constant, mechanical parameters, elastic properties, melting point, and hardness of the  
 17 alloy. Significant tension-compression asymmetry has been found and explained by the strength differential effect during the uniaxial tests.  
 18 Numerous deformation twins and high densities of stacking faults can be observed from the morphological characterization by a transmission  
 19 electron microscope, which governs the main deformation mechanism during the plastic deformation in the current high-entropy alloys.

20 Published under an exclusive license by AIP Publishing. <https://doi.org/10.1063/5.0045414>

## 21 I. INTRODUCTION

22 High-entropy alloys (HEAs) that are mainly defined from the  
 23 viewpoint of composition and configuration entropy have attracted  
 24 widespread attention in the materials community from 2004.<sup>1–3</sup>  
 25 One is that the alloys contain five or more principal elements in an  
 26 equimolar or near-equimolar ratio, and each element accounts for  
 27 5%–35% [atomic percent (at. %)]. The other is that the alloys have  
 28 a value of the configuration entropy at least  $1.5R$  in a random  
 29 chaos system ( $R$  is the gas constant). As soon as they appeared,  
 30 researchers have given them much attention because of their  
 31 unique properties, including high hardness and strength,<sup>4</sup> unique  
 32 corrosion resistance,<sup>5,6</sup> high thermal stability,<sup>7,8</sup> excellent irradiation  
 33 resistance,<sup>9,10</sup> good magnetic properties,<sup>11,12</sup> and outstanding fracture,  
 34 fatigue, and thermoelectric properties.<sup>13–15</sup>

35 It is attractive that some single-phase HEAs that are thermo-  
 36 dynamically metastable can be prepared by mixing multi-principal  
 37 elements. At present, representative HEAs possess exact near-  
 38 equimolar ratios, including body-centered-cubic (BCC) TiZrHfNbTa  
 39 HEA<sup>16</sup> and face-centered-cubic (FCC) CoCrFeMnNi HEA.<sup>17</sup> In con-  
 40 trast, hexagonal close-packed (HCP) HEAs were rarely reported.<sup>18,19</sup>

41 The HEAs with HCP structures mainly consisted of rare-earth ele-  
 42 ments, which presented similar atomic sizes and crystal structures.

43 The HCP HEAs were synthesized by arc-melting taking the com-  
 44 positions of YGdTbDyLu,<sup>20</sup> GdTbDyTmLu,<sup>20</sup> HoDyYGdTb,<sup>21–24</sup>

GdHoLaTbY,<sup>18</sup> ScYLaTiZrHf,<sup>25</sup> GdHoErTbDy,<sup>26</sup> CeGdTbDyHo,<sup>27</sup> Ir<sub>26</sub>Mo<sub>20</sub>Rh<sub>22.5</sub>Ru<sub>20</sub>W<sub>11.5</sub>,<sup>28</sup> Ir<sub>22.5</sub>Mo<sub>20</sub>Rh<sub>20</sub>Ru<sub>25</sub>W<sub>9.5</sub>,<sup>28</sup> AlHfScTiZr,<sup>29</sup> Tb<sub>20.3</sub>Dy<sub>20.7</sub>Ho<sub>20.3</sub>Er<sub>19.7</sub>Tm<sub>19</sub>,<sup>30</sup> and ScTiZrHf.<sup>31</sup> A novel preparation method, the thermal decomposition of single-source precursors, was adopted for the fabrication of IrOsReRhRu HCP HEA.<sup>32</sup>

Overall, most developed HCP HEAs were composed of rare-earth elements, and only a few studies focused on the mechanical behavior, not as thoroughly investigated as in BCC and FCC HEAs. Recently, Qiao *et al.* investigated the strengthening behavior in DyErGdHoLuScTbY, DyGdHoLaTbY, and ErGdHoLaTbY HCP HEAs and found that the solid-solution strengthening (SSS) was weak in rare-earth HCP HEAs compared with that in BCC and FCC HEAs.<sup>18,19</sup> The deformation mechanisms were still not understood clearly up to now. Therefore, one goal of this research is to explore the limit of the number of principal components in rare-earth based HCP HEAs. Moreover, another objective is to investigate the mechanical properties and deformation mechanisms of the newly designed rare-earth based HCP HEA.

## II. RULES OF HCP STRUCTURE HEAs

The phase formation is mainly predicted by the phase diagram for traditional alloys, but the phase diagrams of HEAs with more constituent elements are not available. Hence, several criteria, including the enthalpy of mixing ( $\Delta H_{mix}$ ), entropy of

mixing ( $\Delta S_{mix}$ ), atomic-size difference ( $\delta$ ),<sup>33</sup> valence electron concentration (VEC), and  $\phi$ -parameter based on thermodynamics, were proposed to predict the phase formation in various HEAs. The configurational entropy,  $\Delta S_{conf}$ , can be obtained by

$$\Delta S_{conf} = R \ln N, \quad (1)$$

where  $R$  is the gas constant and  $N$  is the number of elements. Mixing the constituent elements with an equiatomic ratio,  $\Delta S_{mix}$  can reach the maximum value based on Eq. (1). The stability of HEAs is determined by  $\Delta H_{mix}$  and  $\Delta S_{mix}$  together.<sup>17</sup>  $\delta$  and  $\Delta H_{mix}$  are defined as follows:

$$\delta = \sqrt{\sum_{i=1}^N c_i(1 - r_i/\bar{r})^2}, \quad (2)$$

$$\Delta H_{mix} = 4 \sum_{i=1, i \neq j}^n \Delta H_{ij} c_i c_j, \quad (3)$$

where  $c_i$  (and  $c_j$ ) is the atomic fraction of the  $i$ th (and  $j$ th) component,  $r_i$  is the atomic radius of the  $i$ th constituent element, and  $\bar{r} (= \sum c_i r_i)$  is the average atomic radius of the alloy,  $\Delta H_{ij}$  is the mixing enthalpy of a binary liquid alloy, which can be acquired from the empirical model in the liquid state.<sup>34</sup> In addition, Yao *et al.* found that it is preferent for HEAs to form solid solution if the atomic-size difference ( $\delta$ ) is lower than 5.5.<sup>35</sup> Recent studies indicated that HEAs show the single-phase solid solution structures when  $-16.25 \text{ kJ/mol} \leq \Delta H_{ij} \leq \pm 5 \text{ kJ/mol}$ .<sup>36</sup>

The single  $\varphi$ -parameter is defined as<sup>37</sup>

$$\varphi = \frac{\Delta S_{mix} - |\Delta H_{mix}|/T_m}{|S_E|}, \quad (4)$$

where  $S_E$  is the excessive entropy of mixing, which is modeled as a function of atomic size and atomic packing.  $T_m$  is the melting point of the alloy. It is found that the single-phase solid solutions are generally formed for multicomponent HEAs with  $\varphi > \varphi_c$ , and

amorphous phases or multiphases with  $\varphi < \varphi_c$ . Gao *et al.* identified the criteria  $\varphi_c$  with the value of 7.<sup>36</sup> The basis for the formation of a single-phase HEA can be described by these critical parameters ( $\Delta H_{mix}$ ,  $\Delta S_{mix}$ ,  $\delta$ , and  $\varphi$ ). Besides, VEC can be used to judge the phase formation,

$$\text{VEC} = \sum_{i=1}^n c_i(\text{VEC})_i, \quad (5)$$

where  $(\text{VEC})_i$  is the VEC of the  $i$ th element. It is currently believed that the present HEAs possess the HCP structure with  $\text{VEC} \geq 3$ .<sup>37–39</sup> These parameters of different single HCP HEAs together with the ScYLaGdTbDyHoErLu alloy are summarized in Table I. Therefore, it can be inferred that the ScYLaGdTbDyHoErLu alloy can form a single-phase HCP HEA based on these parameters.

### III. EXPERIMENTAL PROCEDURES

Equiatomic ScYLaGdTbDyHoErLu ingots were prepared by vacuum arc melting in the Ti-gettered high-purity argon atmosphere using high-purity elements (weight purity  $\geq 99.9\%$ ). The ingots were remelted six times to ensure the chemical homogeneity. The structures of the alloys were characterized by x-ray diffraction (XRD) using the Cu K $\alpha$  radiation in the  $2\theta$  range of 20°–80°. Optical microscopy (OM) and scanning electron microscopy (SEM) were employed to observe the microstructures of the alloys, and an energy dispersive spectrometer (EDS) was used to analyze chemical compositions. The structures of as-cast and deformed alloys were further analyzed by the JEM-F200 transmission electron microscopy (TEM), selected area electron diffraction (SAED), and high-resolution transmission electron microscopy (HRTEM). The TEM samples were prepared by ion-beam thinning. Elastic properties of the alloys were investigated by resonant ultrasound spectroscopy (RUS) with the rod-like samples under a gauge dimension of  $\phi 3 \times 2.5 \text{ mm}$ . The thermal properties of the alloys were examined by a differential scanning calorimetry (DSC) at a rate of 15 K/min from room temperature (298 K) to 1773 K under a high purity argon atmosphere.

TABLE I. The different thermodynamic parameters of the single HCP HEAs.  $R$  is the gas constant,  $R = 8.314 \text{ J mol}^{-1} \text{ K}^{-1}$ .

Alloys	$S_{conf} (\text{J mol}^{-1} \text{ K}^{-1})$	$\Delta H_{mix} (\text{kJ mol}^{-1})$	$\Delta (\%)$	VEC	$\varphi$	Reference
ScYLaGdTbDyHoErLu	2.20R	0.4	3.4	3	55.1	This work
GdHoLaTbY	1.51R	0	2.2	3	97.5	18
DyGdHoLaTbY	1.79R	0	2.1	3	116.2	19
ErGdHoLaTbY	1.79R	0.1	2.2	3	100.8	19
DyErGdHoLuScTbY	2.1R	0.3	2.8	3	79.1	19
YGdTbDyLu	1.61R	0	1.6	3	245.9	20
GdTbDyTmLu	1.61R	0	1.4	3	18.8	20
HoDyYGdTb	1.61R	0	0.8	3	701.5	21
GdDyErHoTb	1.61R	0	0.9	3	626.6	26
Al <sub>15</sub> Hf <sub>25</sub> Sc <sub>10</sub> Ti <sub>25</sub> Zr <sub>25</sub>	1.55R	-17.5	4.9	3.75	5.8	29
Tb <sub>20.3</sub> Dy <sub>20.7</sub> Ho <sub>20.3</sub> Er <sub>19.7</sub> Tm <sub>19</sub>	1.61R	0	4.8	3	21.3	30
ScTiZrHf	1.38R	4.3	4.3	3.75	18.5	31

The Vickers hardness tests were conducted by a load of 200 g with a dwell time of 15 s. Each sample was measured 12 times, and the average value was taken to ensure the consistency. The tensile samples were cut from the ingots, which were dog-bone-like shape with a gauge dimension of 10 mm in length, 3 mm in width, and 2 mm thick. The compressive testing specimens with a diameter of 3 mm and a height of 6 mm were cut from the ingots by a wire-electrode cutting machine. All the surfaces were grinded and the two end's surface were carefully polished to guarantee acceptable parallelism with an aspect ratio (height/diameter) of 2:1 to an accuracy of 5  $\mu\text{m}$ . It should be pointed out that these samples were not rolled because of the formation of cracks, although the deformation in each pass during the rolling was very low. The strain rates of compression and tension tests were  $5 \times 10^{-4} \text{ s}^{-1}$  and carried out by an Instron 5969 mechanical testing machine. One strain gauge with the size of  $9 \times 3 \text{ mm}$  was pasted on the gauge section of the sample to measure the strain during each tension test. Both the compression and tension tests were done at least three times to make sure the accuracy and repeatability of the results.

## IV. RESULTS

## A. Microstructures

Figure 1(a) shows XRD patterns of the as-cast ScYLaGdTbDyHoErLu alloy. It is obvious that only a set of the HCP structure existed, in agreement with the theoretical prediction, which will be discussed in detail in Sec. V. The lattice parameter of the alloy was determined to be  $a = 0.36 \text{ nm}$ ,  $c = 0.5655 \text{ nm}$ , and  $c/a = 1.5708$ . The lattice constants of the alloy and its constituent elements are summarized in Table II. The OM pictures indicated equiaxed grains in the present ScYLaGdTbDyHoErLu alloy, as shown in the inset of Fig. 1(a).

The average grain size of the ScYLaGdTbDyHoErLu alloy that measured and calculated by OM was  $38 \mu\text{m}$ , which is in accordance with the SEM result, as presented in Fig. 1(b). Employing EDS mapping for a blue-colored rectangular area from Fig. 1(c), it is apparent that the elements distributed uniformly within the grains. The significant differences cannot be detected within the experimental uncertainty ( $\text{Sc}_{11.1}\text{Y}_{11.4}\text{La}_{11.8}\text{Gd}_{11.8}\text{Tb}_{10.6}\text{Dy}_{10.7}\text{Ho}_{10.5}\text{Er}_{11.4}\text{Lu}_{10.7}$ ).

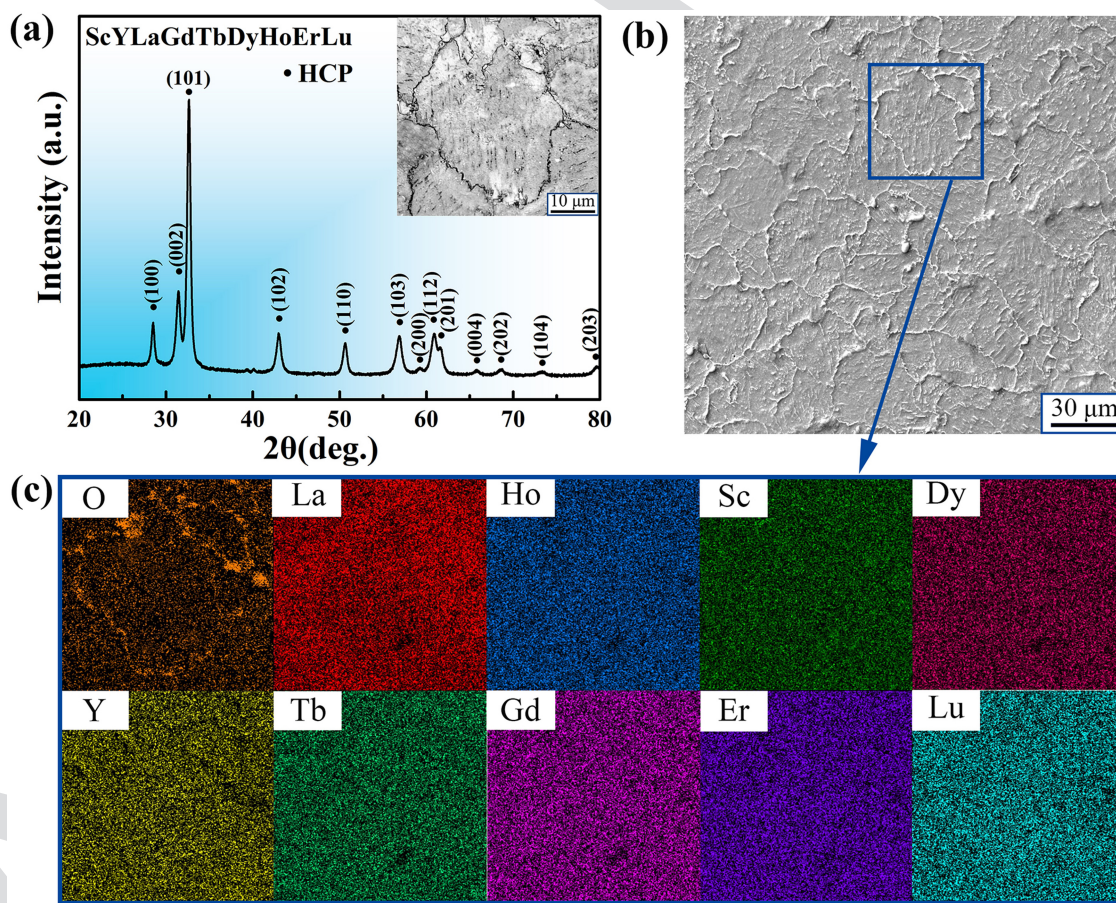


FIG. 1. (a) XRD pattern of the as-cast ScYLaGdTbDyHoErLu HEA. The inset in (a) is the OM image of the current alloy. (b) and (c) show the SEM micrograph and EDS mapping, respectively.

**TABLE II.** Lattice constants,  $a$ ,  $c$ , and  $c/a$  ratios of the ScYLaGdTbDyHoErLu HEA, and single constituent elements. The calculated values are obtained by the RoM.

Alloy and elements		$a$ (nm)	$c$ (nm)	$c/a$
ScYLaGdTbDyHoErLu	Exp. cal.	0.360 0	0.565 5	1.5708
		0.357 8	0.566 2	1.5826
Sc	...	0.330 9	0.527 3	1.5935
Y	...	0.364 74	0.573 06	1.5711
La	...	0.377 2	0.607 2	1.6098
Gd	...	0.363 6	0.578 26	1.5904
Tb	...	0.360 1	0.569 36	1.5811
Dy	...	0.359 3	0.565 37	1.5735
Ho	...	0.357 73	0.561 58	1.5698
Er	...	0.355 88	0.558 74	1.5700
Lu	...	0.350 31	0.555 09	1.5846

similar to the normal composition). Moreover, a strong fluctuation of the elemental distribution was observed at the grain boundary. Each rare-earth element distributed inside the grains homogeneously (~6.9 at. % for each other elements), and some oxygen appeared at the grain boundary. The similar distribution has been reported in previous studies on rare-earth HCP HEAs with precipitates, and the element of oxygen was enriched at grain boundaries as well.<sup>18,19,40</sup> The oxygen was mainly from the raw material due to the exposure during the fabrication and/or transportation of the material, since rare-earth metals and alloys were easily oxidized.

Some small particles can be found within the grains in Fig. 1(b). The content of each element for the particle inclusions were approximately 11.1 at. % in the ScYLaGdTbDyHoErLu alloy. Therefore, the elemental concentration distribution within particles was analogous to that of the matrix. It is worth noted that the dimension of the particles was beyond the resolution limit of the SEM-EDS instrument, which means that the EDS spectrometer readings may contain additional signals from the matrix.

The TEM analysis was employed to further investigate the composition of the particles in the ScYLaGdTbDyHoErLu alloy, as displayed in Fig. 2. The morphologies of the ScYLaGdTbDyHoErLu alloy were island-like in Fig. 2(a), where bright precipitates were embedded in the dark matrix. The size of the precipitates was approximately 1  $\mu\text{m}$ . The elemental composition of the precipitates was studied by TEM-EDS, demonstrating in the upper right corner of Fig. 2(a), with a composition of  $\text{Sc}_{77.96}\text{Lu}_{8.4}\text{Er}_{4.76}\text{Ho}_{2.7}\text{Y}_{2.67}\text{Dy}_{1.36}\text{La}_{0.93}\text{Gd}_{0.77}\text{Tb}_{0.62}$ , which manifests that the precipitates were Sc-rich (~78 at. %). The TEM-EDS mapping that displayed in Fig. 2(e) revealed that the precipitates in the alloy mainly consisted of Sc element, which were in good agreement with the results of Fig. 2(a). The SAED of the precipitates along the  $[1\bar{1}2]$  zone axis was displayed in Fig. 2(c), which corresponds to a BCC structure. In contrast, the XRD pattern in Fig. 1(a) shows that the alloy almost has a single HCP phase, and no sharp peaks corresponding to the BCC phase were captured, because the small size and low volume fraction of the particles were not easily detected by the XRD instrument due to the resolution limit.

Similarly, some precipitates were found in YGdTbDyHo<sup>41</sup> and YGdTbDyLu<sup>20</sup> HEAs as well. The Y-rich precipitates were mainly

located at grain boundaries in YGdTbDyHo HEAs.<sup>41</sup> Takeuchi *et al.* believed that the Ta-rich precipitates were found in the grains of YGdTbDyLu alloys, since Ta was wrapped up by the Lu element as a major impurity.<sup>20</sup> The different enrichment may be attributed to many factors, such as the interaction of different constituent elements and the distinctly forming method, etc. The SAED pattern along the [0001] zone axis of the region A with an HCP structure was shown in Fig. 2(b). The alloy was chemically homogeneous, and there were no precipitates or secondary phases if ignoring the presence of minor particulates inside the grains. In the as-cast ScYLaGdTbDyHoErLu alloy, the twins were observed in Fig. 2(d). These growth twins stemmed from nucleation along the faulted layers during solidification.<sup>42-44</sup> The width of growth twins in the ScYLaGdTbDyHoErLu alloy mostly ranged from 100 to 300 nm.

## B. Mechanical properties

The true stress-strain curve of the ScYLaGdTbDyHoErLu alloy upon quasi-static compression is presented in Fig. 3(a). The compressive yielding strength ( $\sigma_y^c$ ), compressive fracture strength ( $\sigma_f^c$ ), and compressive plastic strain ( $\varepsilon_p^c$ ) for the current ScYLaGdTbDyHoErLu HEA were 251 MPa, 1197 MPa, and 20.2%, respectively. The detailed compressive mechanical properties, the Vickers hardness values of the ScYLaGdTbDyHoErLu HEA and its constituent elements at room temperature are listed in Table III.

In order to explore the mechanical properties of the ScYLaGdTbDyHoErLu HEA, the tensile tests at a strain rate of  $5 \times 10^{-4} \text{ s}^{-1}$  at room temperature were conducted, since the tensile strength was more sensitive to structural defects. The typical true tensile stress-strain curves are displayed in Fig. 3(b). It can be observed that the tensile yielding strength ( $\sigma_y^t$ ) was 213 MPa, the tensile fracture strength ( $\sigma_f^t$ ) was 329 MPa, and the tensile plastic strain ( $\varepsilon_p^t$ ) was 12.2%. It is noted that  $\sigma_f^t$  was much higher than  $\sigma_y^t$  in the current HEA, indicating a distinguishing working-hardening capacity. The formation of working hardening will be discussed in Sec. V.

For the sake of revealing deformation features of the alloy upon quasi-static tensile deformation, TEM was employed to observe the fracture morphology and to investigate the deformation structure in detail. Straight line-like deformation twins (DTs) and growth twins co-existed in the deformed alloy, as clearly observed in Fig. 4. The inset in Fig. 4(b) was the HRTEM image of the straight line-like DTs, and most DTs—with a twin thickness of less than 100 nm except for the thicker growth twins were widely found. As shown in Fig. 4(b), a large number of DTs formed along the growth-twin walls. Meanwhile, the SAED pattern of DTs is shown in Fig. 4(b). This result was generally consistent with previous reports that mechanical twinning was activated during continuous loading in the annealed twin boundaries.<sup>45</sup> Under uniaxial tensile loading, multiplication of dislocations tended to pile up at the boundaries to form dislocation plug groups, resulting in a continuous increase in the local stress between the dislocations and boundaries. When the local stress reached a critical value, the DTs would be activated.

It should be noted that the growth-twin boundaries together with grain boundaries were considered as effective barriers for dislocations. In addition, the dislocation interaction will lead to a higher strain energy on the growth twins compared with the grain.

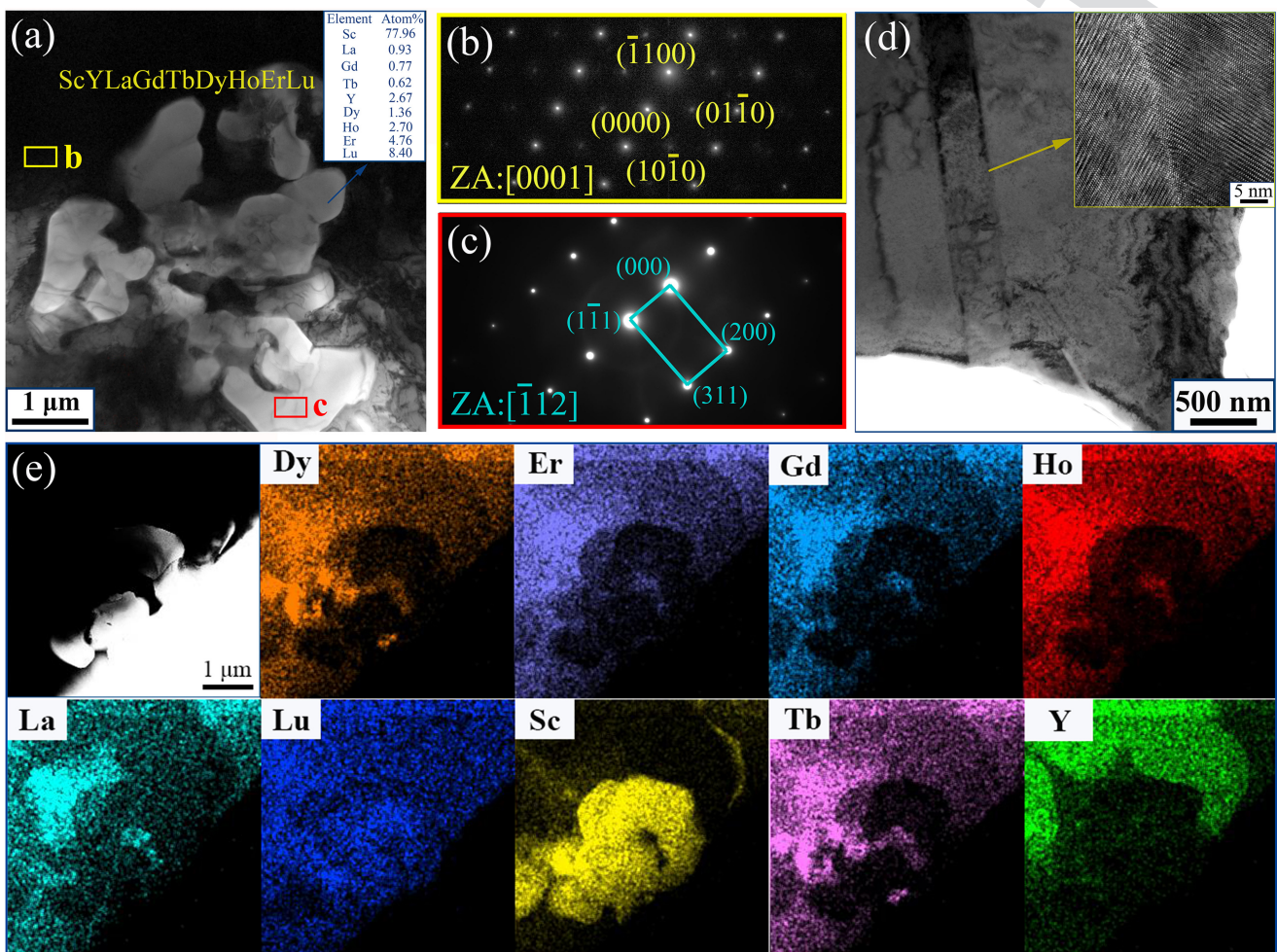


**FIG. 2.** (a) and (b) TEM bright-field images of the ScYLaGdTbDyHoErLu alloy for the as-cast sample in (a) and (d). (b) and (c) show SAED patterns of the precipitation and HCP matrix, respectively. TEM-EDS mappings of precipitation are shown in (e).

Therefore, the growth-twin boundaries acted as preferential sites by analyzing the character of DTs in the ScYLaGdTbDyHoErLu HEA. The HRTEM and inverse fast Fourier transform (IFFT) images of the bottle-shaped red wire frame that marked in Fig. 4(c) were noticeably depicted in Fig. 4(d), which reveals that there were high-density stacking faults (SFs) in the deformed ScYLaGdTbDyHoErLu alloy.

## V. DISCUSSION

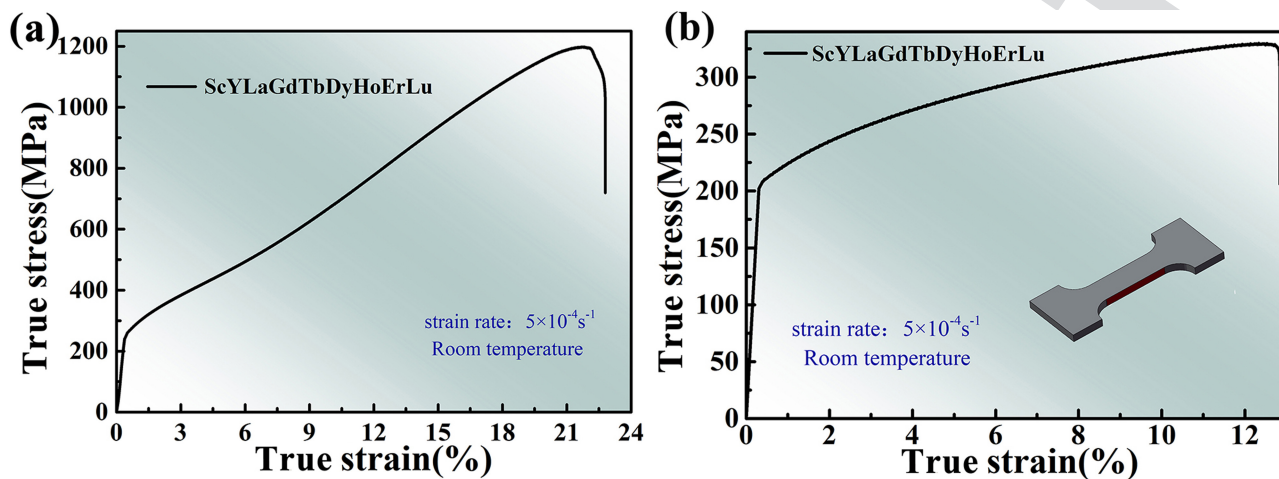
### A. Rule of mixture (RoM)

Figure S1 shows the DSC curve of the ScYLaGdTbDyHoErLu alloy in the [supplementary material](#). A smooth curve with no endothermic or exothermic peaks of the HEA manifested no phase transformation appeared before it was melted. The lowest point of the curve, indicated by the arrow, is the melting point of the alloy. So it can be determined from Fig. S1 that the melting point is

1336 °C for the alloy. The ScYLaGdTbDyHoErLu alloy possesses high thermal stability and keeps the HCP structure all the time before melting. The melting points of the current HEAs and their constituents are listed in [Table IV](#).

Meanwhile, Poisson's ratio ( $\nu$ ), bulk modulus ( $B$ ), Young's modulus ( $E$ ), and shear modulus ( $G$ ) of the alloys and the corresponding constituent elements are summarized in [Table IV](#). The melting point that was calculated by the rule of mixture (RoM) was 1441.6 °C, which substantially matches with the experimental values of 1336 °C. The measured elastic properties ( $B$ ,  $E$ , and  $G$ ) and  $T_m$  were in good agreement with the calculation by RoM. The properties ( $P$ ) can be calculated by

$$P = \sum_{i=1}^n c_i P_i, \quad (6)$$



**FIG. 3.** (a) The compressive true stress–strain curve of the ScYLaGdTbDyHoErLu HEA at room temperature. (b) Loading the tensile true stress–strain curve of the ScYLaGdTbDyHoErLu HEA.

where  $P_i$  is the mechanical property of the constituent element. Poisson's ratio ( $\nu_c$ ) of the alloys can be determined,<sup>36</sup>

$$\nu_c = \frac{3B_c - 2G_c}{2(3B_c + G_c)}, \quad (7)$$

where  $B_c$  and  $G_c$  are the calculated bulk modulus and shear modulus by the RoM, respectively.  $\nu_c$  of the ScYLaGdTbDyHoErLu alloy was 0.27, which is basically the same with the experimental value.

The lattice constants ( $a$ ,  $c$ , and  $c/a$  ratio) of the current ScYLaGdTbDyHoErLu HEA with the constituent elements, and the calculated results by RoM, are listed in Table II. The values exhibited good agreement between the experiment and calculation. The

mechanical properties ( $\sigma_y^c$  and HV) of the alloy do not meet the RoM, as seen from Fig. 3(b) and Table III.

## B. Solid-solution strengthening (SSS)

The Vickers hardness was linearly proportional to the compressive yielding strength, which is benefit of uncovering the strengthening mechanism based on the compressive mechanical properties. The compressive mechanical properties and hardness are summarized in Fig. 5(a). It is obvious that the experimental values have been significantly improved upon the compression yielding strength and hardness, which reveals that the present alloy has undergone vital strengthening effects. The main strengthening in most HEAs is solid-solution strengthening (SSS) since it is hard to distinguish the solute and solvent atoms. Meanwhile, the solute element content is especially high, which leads to the significant SSS results. Currently, the classical Labusch equation has been successfully modified and applied to calculate SSS in HEAs.<sup>46</sup> The value of SSS of the HEAs can be estimated by

$$\Delta\sigma = \left( \sum \Delta\sigma_i^{3/2} \right)^{2/3}, \quad (8)$$

where  $\Delta\sigma_i$  is the SSS value of the  $i$ th component element.  $\Delta\sigma_i$  can be expressed as

$$\Delta\sigma_i = ZGf_i^{4/3}c_i^{2/3}. \quad (9)$$

Here,  $Z$  is a material-dependent dimensionless constant ( $Z = 0.04$ ),<sup>47</sup>  $G$  is the experimental value of the shear modulus of the HEAs, as obtained in Table IV,  $f_i$  is the mismatch parameter, as calculated in detail elsewhere,<sup>19</sup> and  $c_i$  is the atomic fraction of the  $i$ th element.

The SSS value of the current ScYLaGdTbDyHoErLu HEA can be obtained by Eq. (11), which was 53 MPa. The SSS value was greatly enhanced with the increase in constituent elements.

**TABLE III.** The compression properties and hardnesses of the ScYLaGdTbDyHoErLu HEA and their constituent elements. The calculated values for HEAs are achieved by the RoM.

Alloy and elements		HV	$\sigma_y^c$ (MPa)	$\sigma_f^c$ (MPa)	$\epsilon_p^c$ (%)
ScYLaGdTbDyHoErLu	Exp. cal.	164	251	1197	20.2
		98.8	169	878	25.1
Sc	...	73	55	...	...
Y	...	134	280	1065	20.6
La	...	39	90	415	34.2
Gd	...	63	83	677	25
Tb	...	71	140	921	18.6
Dy	...	110	260	823	22.3
Ho	...	127	180	976	24.2
Er	...	130	195	1233	26.9
Lu	...	142	240	915	28.9

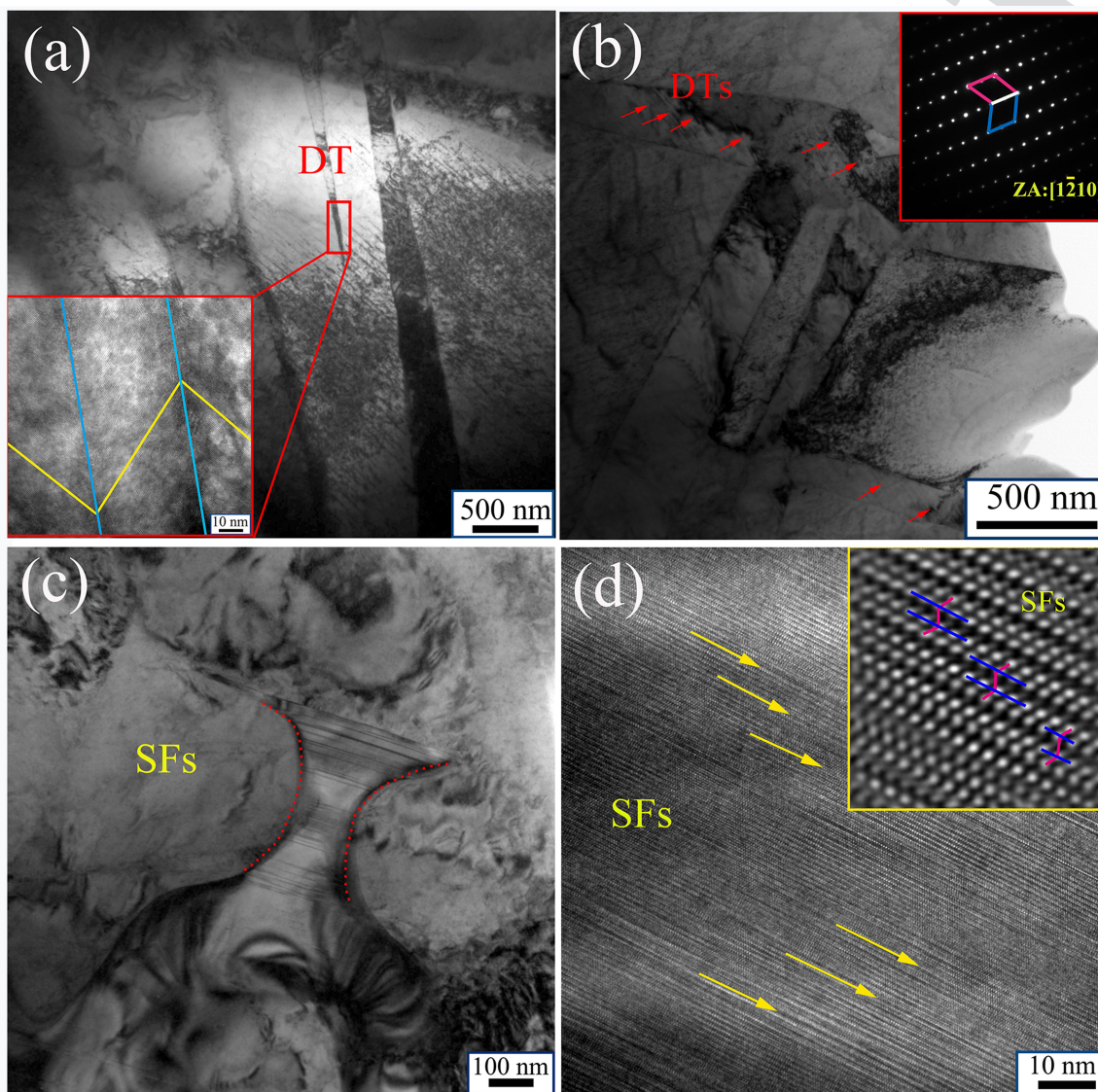


**FIG. 4.** (a)–(c) TEM bright-field images of the ScYLaGdTbDyHoErLu HEA after fracture. The inset in (b) is SADE patterns of TDs (the red arrow). (d) is the HRTEM of the red dashed region of (c). IFFT of the SFs is shown in the inset of (d).

In other words, a large lattice distortion formed a great lattice mismatch in the current rare-earth HEAs. Therefore, the larger value of  $\delta$  is, the more obvious of the SSS can be obtained. More detailed values of  $\delta$  and  $\Delta\sigma$  in the different rare-earth HEAs are shown in Fig. 5(b). The calculated value of the compressive yielding strength ( $\sigma_y^{cal}$ ) can be predicted by the following equation:

$$\sigma_y^{cal} = \sigma_y^{mix} + \Delta\sigma, \quad (10)$$

where  $\sigma_y^{mix}$  is the average yielding strength of the constituent elements by RoM. The  $\sigma_y^{cal}$  value of the alloy was 222 MPa, which was

basically consistent with the experimental values ( $\sigma_y^e$ ) within the allowable range of error. The calculated and experimental yielding strengths of the alloy are displayed in Fig. 5(c). Obviously, the yielding strength of the current HEA can be easily predicted by the SSS model.

### C. Plastic deformation

To achieve the uniform plastic deformation and avoid cracking, according to the Von Mises–Taylor criterion, each grain must satisfy five independent slip systems.<sup>48</sup> Most of HCP alloys cannot meet the Von Mises–Taylor criterion because of lack of

**TABLE IV.** The values of the elastic performance ( $B$ ,  $E$ , and  $G$ ), Poisson's ratio and melting point of the ScYLaGdTbDyHoErLu HEA and constituent elements.

Alloy and elements		Poisson's ratio ( $\nu$ )	Bulk modulus, $B$ (GPa)	Young's modulus, $E$ (GPa)	Shear modulus, $G$ (GPa)	Melting point, $T_m$ (°C)
ScYLaGdTbDyHoErLu	Exp. cal.	0.27 —	45.1 44.9	62.1 63	24.4 24.8	1336 1411.6
Sc	...	0.28	55	73	29	1541
Y	...	0.29	58	72	27	1526
La	...	0.28	27	36	14	920
Gd	...	0.26	36	51	20	1312
Tb	...	0.27	43	58	23	1356
Dy	...	0.24	43	68	27	1407
Ho	...	0.24	42	66	26	1461
Er	...	0.25	48	70	28	1529
Lu	...	0.27	52	73	29	1652

335 independent slip systems at room temperature. Therefore, the  
 336 alloys with the HCP structure need to produce twins or non-basal  
 337 slips to exhibit favorable plasticity.<sup>48</sup>

338 The DTs acted as a carrier of the stress release, which can be  
 339 observed easily in the TEM visualization. Twinning, causing a plenty  
 340 of lattice orientation change, was the main reason that increased the  
 341 c axis strain to improve the plasticity of the alloy. Through character-  
 342 ization of morphologies by TEM, it is found that DTs with a width  
 343 of less than 100 nm was active during plastic deformation, as shown  
 344 in Fig. 4(a). During analysis of the secondary-twins associated with  
 345 the nucleation within the HEAs, it is obvious that the growth-twin  
 346 boundaries were prone to be preferential nucleation sites, as dis-  
 347 played in Fig. 4(b). Furthermore, many SFs were generated within  
 348 the grains in Figs. 4(c) and 4(d). Basically, the micro-twins and new  
 349 twins will be formed due to the multiplication and expansion of SFs  
 350 with the increase in plastic strain.

351 The ratio of  $c/a$  shows significant impacts on the different  
 352 types of slip, and the ideal value of the perfect stacking model of  
 353 HCP structures is  $c/a = 1.633$ . The ratios are lower than the ideal  
 354 values in Ti alloys, which manifests that the deformation

355 mechanism is dominated by the prismatic  $\langle a \rangle$  slip.<sup>49</sup> Moreover, the  
 356 basal  $\langle a \rangle$  slip is treated as the governed deformation mechanism in  
 357 Mg, Zn, and Cd alloys when the ratios are close or higher than the  
 358 ideal values.<sup>49</sup> The axial ratio is reduced in the HCP alloys, which  
 359 makes the non-basal slip easy to be activated. In this case, the acti-  
 360 vation stress will be increased for the basal slip and decreased for the  
 361 prismatic and pyramidal slip.<sup>50</sup> Similarly, the recent studies  
 362 have shown that the ratio of  $c/a$  has been tuned into regimes to  
 363 promote the activation of non-basal slips in HEAs.<sup>24</sup>

364 It is reasonable to speculate that the ScYLaGdTbDyHoErLu  
 365 alloy can produce a large number of the non-basal slip with the  
 366 axial ratio of 1.571, which is lower than the ideal value of 1.633.  
 367 The schematic diagram of the microstructure evolution in the  
 368 ScYLaGdTbDyHoErLu alloy during tensile deformation is pre-  
 369 sented in Fig. 6. The non-basal slip will be activated after yielding.  
 370 With the increase in the strain, the multiplication and expansion of  
 371 SFs appeared in the localized growth twins. The DTs will be nucle-  
 372 ated as soon as the overlap of SFs reached a critical density. Such a  
 373 critical arrangement was preferentially observed within the active  
 374 DTs, which were located adjacent to growth-twin boundaries.

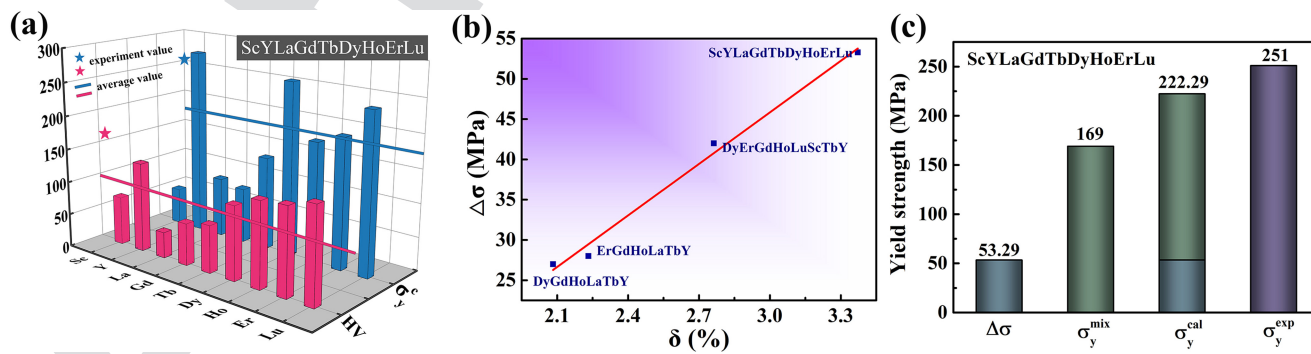
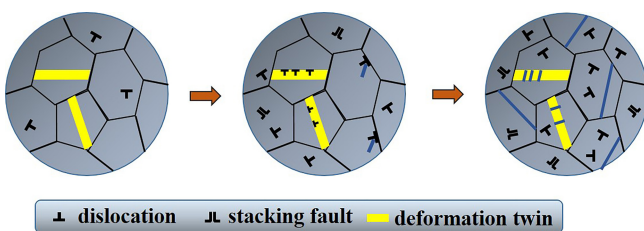


FIG. 5. (a) The measured compression mechanical properties (HV,  $\sigma_y^c$ ) of the HEAs. Pentagrams represent the experimental values, and the solid lines represent the calculated values by the RoM. (b) Comparison between experiments and calculations on the compressive yield strength. (c)  $\delta$  and  $\Delta\sigma$  values of rare-earth HEAs with the single-phase HCP structure.



**FIG. 6.** The deformation processes of the ScYLaGdTbDyHoErLu HEA under quasi-static tensile.

375 It is obvious that the asymmetry between tensile and compressive 376 yielding of the ScYLaGdTbDyHoErLu alloy appeared, which is 377 related to the strength differential (SD) effect. The compressive and 378 tensile yielding strength of the alloy were 251 and 213 MPa, respectively. The SD-parameter can be defined as<sup>51,52</sup>

$$SD = 2 \frac{|CYS| - |TYS|}{|CYS| + |TYS|}, \quad (11)$$

380 where *CYS* and *TYS* represent the compressive yielding stress and 381 tensile yielding stress, respectively. *CYS* was slightly higher than the 382 *TYS* in the ScYLaGdTbDyHoErLu alloy, and the *SD* value was 383 0.1638. In other words, the tension-compression yielding asymmetry 384 of the alloy existed under the uniaxial stress state at room 385 temperature.

386 Generally, the tension-compression yielding asymmetry phe- 387 nomenon has been widely reported in many traditional alloys, such 388 as magnesium alloys<sup>53,54</sup> and aluminum alloys.<sup>55</sup> The pronounced 389 negative SD effect takes place in most conventional alloys in which 390 the *CYS* is significantly lower than the *TYS*.<sup>51,56</sup> This rare-earth 391 based HEA has nonequivalent families of slip systems, since the 392 HCP structure is geometrically anisotropic and the critical resolved 393 shear stress on the slip system changes considerably. Compared 394 with FCC or BCC alloys, the current HCP HEA deformed by slip 395 and twinning during the plastic deformation. Different from non- 396 directional slips, twinning is more sensitive to the shear direction, 397 which means the twinning can be active in one direction but not 398 activated in the opposite direction. According to the TEM results, a 399 large number of DTs can be observed after fracture. The DTs will 400 be activated during the plastic deformation due to the high level of 401 local stress. In the current HCP HEA, the basal slip and twinning 402 played a more significant role in the compression tests. However, 403 the basal slip and non-basal slip were regarded as the main defor- 404 mation mechanism in tension.<sup>57</sup> The higher *CYS* was obtained 405 because of the difference of critical activation stress of non-basal 406 slips and twinning, which results in the asymmetry in tension and 407 compression tests.

## 408 VI. CONCLUSIONS

409 In summary, a novel ScYLaGdTbDyHoErLu alloy with a 410 single HCP structure was designed, as predicted by the proposed 411 parameters, including  $\Delta H_{mix}$ ,  $\Delta S_{mix}$ ,  $\delta$ , VEC, and  $\varphi$ -parameter. The

microstructures and mechanical properties were investigated in detail, from which the main conclusions were obtained as follows:

- (1) The thermodynamic parameters were used to preliminarily predict the single HCP phase of the ScYLaGdTbDyHoErLu rare-earth based HEA, which was verified by SEM and TEM characterization.
- (2) The lattice constants, melting point, and elastic properties (bulk modulus, Young's modulus, and shear modulus) of the ScYLaGdTbDyHoErLu alloy that were obtained were in accordance with the RoM. The hardness and compressive yielding strength that calculated by RoM were higher than the experimental values, which reveals the obvious strengthening effect.
- (3) The compressive yielding strength of the HEA can be well predicted by the SSS model. The value of  $\Delta\sigma$  of the ScYLaGdTbDyHoErLu alloy was 53.29 MPa. The solid-solution strengthening effect will be stronger due to the increase in compositional element or difference in atomic radii.
- (4) A large number of SFs and DTs nucleated from the growth-twin boundaries by observing the morphologies of tensile specimens. The asymmetry phenomenon was characterized by the positive *SD* parameter, since the compressive yielding strength was higher than the tensile yielding strength in the current HEA.

## SUPPLEMENTARY MATERIAL

See the supplementary material for the DSC curve of the ScYLaGdTbDyHoErLu HEA. The melting point of the current alloy was marked by the red arrow in Fig. S1.

## AUTHORS' CONTRIBUTIONS

Z.W. and M.L.B. contributed equally to this work.

## ACKNOWLEDGMENTS

J.W.Q. would like to acknowledge financial support of the Natural Science Foundation of Shanxi Province, China (Nos. 201901D111105 and 201901D111114); Transformation of Scientific and Technological Achievements Programs of Higher Education Institutions in Shanxi (2019); and the opening project of the State Key Laboratory of Explosion Science and Technology (Beijing Institute of Technology), opening Project No. KFJJ20-13M. Z.W. would like to acknowledge financial support of the China Postdoctoral Science Foundation (No. 2020M670708). P.K.L. very much appreciates support of the U.S. Army Research Office Project (Nos. W911NF-13-1-0438 and W911NF-19-2-0049) with program managers Dr. M. P. Bakas, Dr. S. N. Mathaudhu, and Dr. D. M. Stepp. P.K.L. acknowledges support from the National Science Foundation (NSF) (Nos. DMR-1611180 and 1809640) with program directors Dr. J. Yang, Dr. J. G. Shiflet, and Dr. D. Farkas.

## DATA AVAILABILITY

The data that support the findings of this study are available from the corresponding author upon reasonable request.

## 460 REFERENCES

- <sup>461</sup> <sup>1</sup>J.-W. Yeh, S.-K. Chen, S.-J. Lin, J.-Y. Gan, T.-S. Chin, T.-T. Shun, C.-H. Tsau, and S.-Y. Chang, *Adv. Eng. Mater.* **6**, 299 (2004).
- <sup>462</sup> <sup>2</sup>B. Cantor, I. T. H. Chang, P. Knight, and A. J. B. Vincent, *Mater. Sci. Eng. A* **464**, 375–377, 213 (2004).
- <sup>463</sup> <sup>3</sup>Y. Zhang, T. T. Zuo, Z. Tang, M. C. Gao, K. A. Dahmen, P. K. Liaw, and Z. P. Lu, *Prog. Mater. Sci.* **61**, 1 (2014).
- <sup>464</sup> <sup>4</sup>J. Y. He, W. H. Liu, H. Wang, Y. Wu, X. J. Liu, T. G. Nieh, and Z. P. Lu, *Acta Mater.* **62**, 105 (2014).
- <sup>465</sup> <sup>5</sup>Y. Shi, B. Yang, X. Xie, J. Brechtl, K. A. Dahmen, and P. K. Liaw, *Corros. Sci.* **119**, 33 (2017).
- <sup>466</sup> <sup>6</sup>Y. Shi, L. Collins, R. Feng, C. Zhang, N. Balke, P. K. Liaw, and B. Yang, *Corros. Sci.* **133**, 120 (2018).
- <sup>467</sup> <sup>7</sup>H. W. Yao, J. W. Qiao, J. A. Hawk, H. F. Zhou, M. W. Chen, and M. C. Gao, *J. Alloys Compd.* **696**, 1139 (2017).
- <sup>468</sup> <sup>8</sup>Y. Zou, J. M. Wheeler, H. Ma, P. Okle, and R. Spolenak, *Nano Lett.* **17**, 1569 (2017).
- <sup>469</sup> <sup>9</sup>M. W. Ullah, D. S. Aidhy, Y. Zhang, and W. J. Weber, *Acta Mater.* **109**, 17 (2016).
- <sup>470</sup> <sup>10</sup>O. El-Atwani, N. Li, M. Li, A. Devaraj, J. K. S. Baldwin, M. M. Schneider, D. Sobieraj, J. S. Wróbel, D. Nguyen-Manh, and S. A. Maloy, *Sci. Adv.* **5**, eaav002 (2019).
- <sup>471</sup> <sup>11</sup>Y. Yuan, Y. Wu, X. Tong, H. Zhang, H. Wang, X. J. Liu, L. Ma, H. L. Suo, and Z. P. Lu, *Acta Mater.* **125**, 481 (2017).
- <sup>472</sup> <sup>12</sup>T. Zuo, M. C. Gao, L. Ouyang, X. Yang, Y. Cheng, R. Feng, S. Chen, P. K. Liaw, J. A. Hawk, and Y. Zhang, *Acta Mater.* **130**, 10 (2017).
- <sup>473</sup> <sup>13</sup>B. Gludovatz, A. Hohenwarter, D. Catoor, E. H. Chang, E. P. George, and R. O. Ritchie, *Science* **345**, 1153 (2014).
- <sup>474</sup> <sup>14</sup>Z. Tang, T. Yuan, C.-W. Tsai, J.-W. Yeh, C. D. Lundin, and P. K. Liaw, *Acta Mater.* **99**, 247 (2015).
- <sup>475</sup> <sup>15</sup>Z. Fan, H. Wang, Y. Wu, X. Liu, and Z. Lu, *Mater. Res. Lett.* **5**, 187 (2017).
- <sup>476</sup> <sup>16</sup>O. N. Senkov, J. M. Scott, S. V. Senkova, D. B. Miracle, and C. F. Woodward, *J. Alloys Compd.* **509**, 6043 (2011).
- <sup>477</sup> <sup>17</sup>F. Otto, Y. Yang, H. Bei, and E. P. George, *Acta Mater.* **61**, 2628 (2013).
- <sup>478</sup> <sup>18</sup>Y. J. Zhao, J. W. Qiao, S. G. Ma, M. C. Gao, H. J. Yang, M. W. Chen, and Y. Zhang, *Mater. Des.* **96**, 10 (2016).
- <sup>479</sup> <sup>19</sup>J. W. Qiao, M. L. Bao, Y. J. Zhao, H. J. Yang, Y. C. Wu, Y. Zhang, J. A. Hawk, and M. C. Gao, *J. Appl. Phys.* **124**, 195101 (2018).
- <sup>480</sup> <sup>20</sup>A. Takeuchi, K. Amiya, T. Wada, K. Yubuta, and W. Zhang, *JOM* **66**, 1984 (2014).
- <sup>481</sup> <sup>21</sup>M. Feuerbacher, M. Heidelmann, and C. Thomas, *Mater. Res. Lett.* **3**, 1 (2015).
- <sup>482</sup> <sup>22</sup>F. Yu, L. J. Zhang, J. L. Ning, M. Z. Ma, X. Y. Zhang, Y. C. Li, P. K. Liaw, G. Li, and R. P. Liu, *Mater. Lett.* **196**, 137 (2017).
- <sup>483</sup> <sup>23</sup>J. Lužník, P. Koželj, S. Vrtník, A. Jelen, Z. Jagličić, A. Meden, M. Feuerbacher, and J. Dolinský, *Phys. Rev. B* **92**, 224201 (2015).
- <sup>484</sup> <sup>24</sup>Y. Bu, Z. Li, J. Liu, H. Wang, D. Raabe, and W. Yang, *Phys. Rev. Lett.* **122**, 075502 (2019).
- <sup>485</sup> <sup>25</sup>A. Takeuchi, K. Amiya, T. Wada, and K. Yubuta, *Intermetallics* **69**, 103 (2016).
- <sup>486</sup> <sup>26</sup>Y. Yuan, Y. Wu, X. Tong, H. Zhang, H. Wang, X. J. Liu, L. Ma, H. L. Suo, and Z. P. Lu, *Acta Mater.* **125**, 481 (2017). 510
- <sup>487</sup> <sup>27</sup>S. Vrtník, J. Lužník, P. Koželj, A. Jelen, J. Luzar, Z. Jagličić, A. Meden, M. Feuerbacher, and J. Dolinský, *J. Alloys Compd.* **742**, 877 (2018). 511
- <sup>488</sup> <sup>28</sup>A. Takeuchi, T. Wada, and H. Kato, *Mater. Trans.* **60**, 1666 (2019). 512
- <sup>489</sup> <sup>29</sup>L. Rogal, P. Bobrowski, F. Kormann, S. Divinski, F. Stein, and B. Grabowski, *Sci. Rep.* **7**, 2209 (2017). 513
- <sup>490</sup> <sup>30</sup>M. Krnel, S. Vrtník, A. Jelen, P. Koželj, Z. Jagličić, A. Meden, M. Feuerbacher, and J. Dolinský, *Intermetallics* **117**, 106680 (2020). 514
- <sup>491</sup> <sup>31</sup>S. Uporov, S. K. Estemirova, V. A. Bykov, D. A. Zamyatin, and R. E. Ryltsev, *Intermetallics* **122**, 106802 (2020). 515
- <sup>492</sup> <sup>32</sup>K. V. Yusenko, S. Riva, P. A. Carvalho, M. V. Yusenko, S. Arnaboldi, A. S. Sukhikh, M. Hanfland, and S. A. Gromilov, *Scr. Mater.* **138**, 22 (2017). 516
- <sup>493</sup> <sup>33</sup>Y. Zhang, Y. J. Zhou, J. P. Lin, G. L. Chen, and P. K. Liaw, *Adv. Eng. Mater.* **10**, 534 (2008). 517
- <sup>494</sup> <sup>34</sup>A. Takeuchi and A. Inoue, *Mater. Trans.* **46**, 2817 (2005). 518
- <sup>495</sup> <sup>35</sup>K. Yao, L. Liu, J. Ren, Y. Guo, Y. Liu, Y. Cao, R. Feng, F. Wu, J. Qi, and J. Luo, *Scr. Mater.* **194**, 113674 (2021). 519
- <sup>496</sup> <sup>36</sup>M. C. Gao, P. Gao, J. A. Hawk, L. Ouyang, D. E. Alman, and M. Widom, *J. Mater. Res.* **32**, 3627 (2017). 520
- <sup>497</sup> <sup>37</sup>Y. F. Ye, Q. Wang, J. Lu, C. T. Liu, and Y. Yang, *Scr. Mater.* **104**, 53 (2015). 521
- <sup>498</sup> <sup>38</sup>M. G. Poletti and L. Battezzati, *Acta Mater.* **75**, 297 (2014). 522
- <sup>499</sup> <sup>39</sup>S. Guo, C. Ng, J. Lu, and C. T. Liu, *J. Appl. Phys.* **109**, 103505 (2011). 523
- <sup>500</sup> <sup>40</sup>R. Djenanovic, A. Sarkar, O. Clemens, C. Lohö, M. Botros, V. S. K. Chakravadhanula, C. Kübel, S. S. Bhattacharya, A. S. Gandhi, and H. Hahn, *Mater. Res. Lett.* **5**, 102 (2017). 524
- <sup>501</sup> <sup>41</sup>R. Soler, A. Evirgen, M. Yao, C. Kirchlechner, F. Stein, M. Feuerbacher, D. Raabe, and G. Dehm, *Acta Mater.* **156**, 86 (2018). 525
- <sup>502</sup> <sup>42</sup>D. Bufford, Y. Liu, J. Wang, H. Wang, and X. Zhang, *Nat. Commun.* **5**, 4864 (2014). 526
- <sup>503</sup> <sup>43</sup>Y. M. Wang, F. Sansoz, T. LaGrange, R. T. Ott, J. Marian, T. W. Barbee, Jr., and A. V. Hamza, *Nat. Mater.* **12**, 697 (2013). 527
- <sup>504</sup> <sup>44</sup>M. Gong, J. P. Hirth, Y. Liu, Y. Shen, and J. Wang, *Mater. Res. Lett.* **5**, 449 (2017). 528
- <sup>505</sup> <sup>45</sup>M. Wang, Z. Li, and D. Raabe, *Acta Mater.* **147**, 236 (2018). 529
- <sup>506</sup> <sup>46</sup>R. Labusch, *Phys. Status Solidi B* **41**, 659 (1970). 530
- <sup>507</sup> <sup>47</sup>V. Navratil, M. Hamersky, P. Lukac, V. P. Soldatov, and V. I. Startsev, *Phys. Status Solidi A* **75**, K133 (1983). 531
- <sup>508</sup> <sup>48</sup>M. H. Yoo, *Metall. Trans.* **12**, 409 (1981). 532
- <sup>509</sup> <sup>49</sup>P. G. Partridge, *Int. Mater. Rev.* **12**, 169 (1967). 533
- <sup>510</sup> <sup>50</sup>A. Urakami and M. E. Fine, *Acta Metall.* **19**, 887 (1971). 534
- <sup>511</sup> <sup>51</sup>M. Huppmann, S. Gall, S. Müller, and W. Reimers, *Mater. Sci. Eng. A* **528**, 342 (2010). 535
- <sup>512</sup> <sup>52</sup>T. B. Stoughton and J.-W. Yoon, *Int. J. Plast.* **20**, 705 (2004). 536
- <sup>513</sup> <sup>53</sup>W. Rong, Y. Zhang, Y. Wu, Y. Chen, M. Sun, J. Chen, and L. Peng, *Mater. Sci. Eng. A* **740–741**, 262 (2019). 537
- <sup>514</sup> <sup>54</sup>J. Hao, J. Zhang, C. Xu, and Y. Zhang, *Mater. Sci. Eng. A* **735**, 99 (2018). 538
- <sup>515</sup> <sup>55</sup>J. K. Holmen, B. H. Frodal, O. S. Hopperstad, and T. Børvik, *Int. J. Plast.* **99**, 144 (2017). 539
- <sup>516</sup> <sup>56</sup>M. Huppmann and W. Reimers, *Int. J. Mater. Res.* **101**, 1264 (2010). 540
- <sup>517</sup> <sup>57</sup>M. R. Barnett, *Mater. Sci. Eng. A* **464**, 1 (2007). 541